ECS Journal of Solid State Science and Technology

OPEN ACCESS

Effective Bandstructure Model for Monte Carlo Simulations of Electron and Hole Transport in Germanium

To cite this article: Aynul Islam *et al* 2025 *ECS J. Solid State Sci. Technol.* **14** 073007

View the article online for updates and enhancements.

You may also like

- Combinatorial Corrosion Studies of PVD Deposited, Thermally Interdiffused, Magnesium Coated Galvanized Steel
Zak Barrett, Hamilton N. McMurray and Geraint Williams

- Rubber and rubber-like materials, finite-element analyses and simulations: a bibliography (1976-1997)
Jaroslav Mackerle

- Investigation into the effects of surface stripping ZnO nanosheets
Chris J Barnett, Georgina Jackson, Daniel R Jones et al.

ECC-Opto-10 Optical Battery Test Cell:
Visualize the Processes Inside Your Battery!

Battery Test Cell for Optical Characterization
Designed for light microscopy, Raman spectroscopy and XRD.

Optimized, Low Profile Cell Design (Device Height 21.5 mm)
Low cell height for high compatibility, fits on standard samples stages.

High Cycling Stability and Easy Handling
Dedicated sample holders for different electrode arrangements included!

Cell Lids with Different Openings and Window Materials Available

Contact us:
+49 40 79012-734
sales@el-cell.com
www.el-cell.com

Sample Test (Side-by-Side Setup)

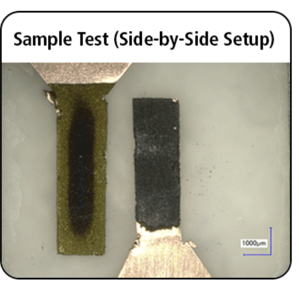

Sample Test (Face-to-Face Setup)

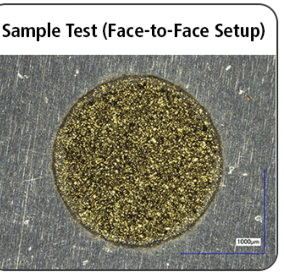

This content was downloaded from IP address 109.155.195.43 on 24/07/2025 at 16:55

ECS Journal of Solid State Science and Technology, 2025 **14** 073007

Effective Bandstructure Model for Monte Carlo Simulations of Electron and Hole Transport in Germanium

Aynul Islam,[1] Shuqiao Cai,[2] Murad Alabdullah,[3,4] and Karol Kalna[3,z]

[1]*Electronics and Electrical Engineering, Glasgow College, UESTC, China, University of Glasgow, Glasgow, G12 8QQ, Scotland, United Kingdom*
[2]*James Watt School of Engineering, University of Glasgow, Glasgow, G12 8LT, Scotland, United Kingdom*
[3]*Nanoelectronic Devices Computational Group, Department of Electronic & Electrical Engineering, Faculty of Science & Engineering, Swansea University, Swansea, SA1 8EN, Wales, United Kingdom*
[4]*Dept. Electronic Techniques, Kirkuk Technical Institute, Northern Technical University, Kirkuk, Iraq*

A simple yet highly effective band structure model of germanium (Ge) for electron and hole transport in bulk semiconductor is developed for Monte Carlo (MC) simulations at 300 K. The simulated electron and hole drift velocities versus the applied electric field are compared with experimental data, serving as a reference for model accuracy. The comparison between the experimental and simulation results, up to an electric field of 700 kV cm^{-1} for electrons and up to 10 kV cm^{-1} for holes in the Ge ⟨100⟩ crystallographic orientation, demonstrates exceptionally good agreement, especially for holes, when compared to previous works. We have found that electron/hole effective masses in the lowest valley (the *L*-valley)/band (the heavy-band) are highly anisotropic with longitudinal and transverse masses of 1.588/1.64 and 0.082/0.052, respectively. The electron and hole mobilities as a function of ionised impurity concentration are also obtained using a static screening model in carrier scattering with ionised impurities. Finally, the relaxation times and the occupation of valleys in the conduction and valence bands are shown as a function of the applied electric field.
© 2025 The Author(s). Published on behalf of The Electrochemical Society by IOP Publishing Limited. This is an open access article distributed under the terms of the Creative Commons Attribution 4.0 License (CC BY, https://creativecommons.org/licenses/by/4.0/), which permits unrestricted reuse of the work in any medium, provided the original work is properly cited. [DOI: 10.1149/2162-8777/adedb7]

Manuscript submitted June 16, 2025; revised manuscript received July 2, 2025. Published July 23, 2025.

A simple band structure model for highly effective ensemble Monte Carlo (MC) simulations is presented for electron and hole transport in bulk germanium (Ge). The accuracy of the model is tested against experimental data[1,2] for the electron and hole drift velocities (v_d), respectively, in high-purity Ge as a function of the applied electric field parallel to the ⟨100⟩ crystallographic orientation at 300 K. Although MC simulations of electron and hole transport in bulk Ge have been reported a few times before,[3–5] we have developed a band structure model that is both simple and highly accurate in reproducing the drift velocity at 300 K, making it particularly suitable for use in time-demanding 3D finite element MC device simulations of electron and hole transport in *n*-type and *p*-type nanoscale multigate field-effect transistors (FETs) such as FinFETs, nanowire FETs, and nanosheet FETs.[6–8] Our analytical model improves the accuracy of reproducing electron drift velocity at high electric fields (around 40–50 kV cm^{-1}) compared to previous full-band simulations.[5] It also enhances the accuracy of reproducing hole drift velocity from around 3 kV cm^{-1} when compared to **k.p** MC simulations.[9] Simulations of electron and hole transport in Ge are essential to advance the performance of nanoscale Si FETs because the performance of *p*-FETs often lags behind the performance of *n*-FETs in complementary metal-oxide-semiconductor (CMOS) technology aimed at logic applications.[10,11] While such MC simulations often treat electrons and holes separately in unipolar devices, the multiparticle MC technique can be readily extended to simulate electron and hole transport in bipolar devices, such as bipolar transistors[12] or solar cells,[13] where superparticles representing electrons and holes undergo free flights and scattering events simultaneously.

Ge exhibits excellent bulk hole mobility of 1900 cm^2/Vs compared to silicon (Si),[14–16] while its electron mobility of 3900 cm^2/Vs is equally competitive. Moreover, Ge is being studied for heterostructure designs that combine Ge with Si in transistor channels to enhance carrier mobility,[17] or for use in critical regions (such as quantum wells) to reduce resistance. This is due to Ge compatibility with existing Si fabrication processes.[18,19] The potential of Ge in *n*-channel and *p*-channel MOSFETs has been hindered by a low interface quality with dielectric layers and the inability to activate sufficiently high doping in the source/drain regions despite some recent encouraging results.[17] Recently, Ge and high-Ge-content channel nanosheet and nanowire FETs have been reported, demonstrating excellent performance as tunnel FETs,[20] reconfigurable FETs,[21] nanosheet ferromagnetic FETs,[22] and nanowire FETs.[23,24]

The hole bulk MC simulations were pioneered by simulations of the hole drift velocity as a function of applied electric field and mobility versus lattice temperature for Si ⟨100⟩, ⟨110⟩, and ⟨111⟩ crystallographic orientations.[25] These hole MC simulations of Si considered two different analytical bandstructures of the valence band: (i) a two-band model consisting of a spherical non-parabolic heavy hole (HH) band and a spherical parabolic light hole (LH) band and (ii) a one-band model consisting of a warped parabolic HH band only. The hole bulk simulations of Ge were followed by simulating the hole drift velocity up to large electric fields of 10^4 V/cm while accounting for the anisotropy in Ge crystals.[26] These MC simulations considered a single warped parabolic HH band model, which neglects transport contributions from the LH band. Later, more advanced MC simulations reported drift velocity, mobility, and average kinetic energy.[3] This MC simulations considered a single warped non-parabolic HH band model neglecting again light-hole band contribution. Finally, the contribution of the spin-orbit band to the hole transport has been neglected or approximated in all previous MC simulations of hole transport in Si and Ge. Later, the hole bulk MC simulations advanced into full band MC simulations in which the semiconductor bandstructure is fully numerically calculated for conduction and valence bands in the Brillouin zone. The bandstructure calculations may use a **k.p** method[9,27] or non-local empirical pseudopotentials[28,29] approach. However, the full band MC simulations are time consuming and can make device simulations extremely long, especially when performed in the 3D real device domain.[30]

Bandstructure Model of Electrons and Holes for Germanium

The band structure of a semiconductor, which is of interest in transport problems, is centred around the energy gap, E_G. This

[z]E-mail: k.kalna@swansea.ac.uk

energy region for the face-centred cubic lattice structure will have several energy points of significance in the conduction and valence bands. These energy points, called valleys, are typically located at the Γ-valley [$\mathbf{k} = (0, 0, 0)$], at the L-valley [$\mathbf{k} = (\pi/a_0, \pi/a_0, \pi/a_0)$, a_0 being the lattice parameter], and along the Δ-valley [$\mathbf{k} = (2\pi/a_0, 0, 0)$; $(0, 2\pi/a_0, 0)$; and $(0, 0, 2\pi/a_0)$]. When the significant energy points or valleys are determined, a description of energy dispersion relation, which determines the relation between wavevector $\mathbf{k}$ and energy E, around these valleys is needed. Efficient ensemble MC simulations require an analytical description of the energy dispersion relation to significantly speed up simulation time, particularly when simulating carrier transport in nanoscale semiconductor devices.

Carriers may be treated in a parabolic band approximation as long as they do not have a very large kinetic energy. In other words, we assume that the holes behave as free particles having a single effective mass regardless of a wavevector component or a crystal orientation. Their energy dispersion is approximated by a parabolic dispersion so that the kinetic energy close to conduction band minimum is a quadratic function of $\mathbf{k}$. The parabolic spherical band model (an isotropic model) represents the relationship between the carrier energy $E_{\mathbf{k}}$ and the crystal momentum $\mathbf{k}$.[31] When the band minimum occurs at $\mathbf{k} = 0$, the energy dispersion relation E_k can be written as:[32]

$$E(\mathbf{k}) = \frac{\mathbf{p}^2}{2m^*} = \frac{\hbar^2\mathbf{k}^2}{2m^*}, \qquad [1]$$

and the connection to classical kinetics through the particle momentum $\mathbf{p}$ is brought to mind. In Eq. 1, m^* is the effective carrier mass defined at the band edge, and $\hbar$ is the Planck constant divided by 2π. The parabolic isotropic bandstructure model at the significant energy point in Brillouin zone (Γ, L, or X, etc.) describes a band whose constant energy surfaces in the $\mathbf{k}$-space are spheres, and whose effective masses in each crystallographic orientation are equal. Equation 1 represents a band with spherical equi-energetic surfaces with a single scalar effective mass m^*, appropriate for the energy minimum of the conduction band (conduction band minimum) and for the energy minimum of the valence band (valence band minimum). Note that the energy minimum of valence band is reverse with respect to the energy of conduction band.

A band with ellipsoidal equi-energetic surfaces is illustrated in Fig. 1. The conduction band energy description uses a tensor effective mass with the effective longitudinal electron mass ($m^*_{e\,\text{long}}$) and with the transverse components of effective electron mass ($m^*_{e\,\text{tran}}$) given by:

$$E(\mathbf{k}) = \frac{\hbar^2}{2}\left(\frac{\mathbf{k}^2_{\text{long}}}{m_e^{*\,\text{long}}} + \frac{\mathbf{k}^2_{\text{tran}}}{m_e^{*\,\text{tran}}}\right), \qquad [2]$$

where $\mathbf{k}_{\text{long}}$ is the longitudinal wave vector and $\mathbf{k}_{\text{tran}}$ is the transverse wave vector. The same expression can be written for valence band energy and holes using effective hole mass (longitudinal and transverse). The ellipsoids have a rotational symmetry around the crystallographic directions which contain the centre of the valleys. This case is often also appropriate for the minima of the conduction band at the L point and along the Δ-valley, but could be used sometimes even at the Γ-valley (in a Si analytical bandstructure[33]). This approximation is often called a parabolic anisotropic bandstructure model.

The energy $E_{\mathbf{k}}$ and the crystal momentum $\mathbf{k}$ for heavy holes in the Γ-valley are treated within the parabolic anisotropic bandstructure model where the constant energy surfaces in $\mathbf{k}$-space are assumed to be ellipsoidal. Consequently, the effective mass m^* becomes a tensor characterised by the longitudinal heavy hole effective mass ($m_{hh}^{*\text{long}}$) and the transverse heavy hole effective mass ($m_{hh}^{*\text{tran}}$). This allows us to express the parabolic anisotropic energy dispersion relation as:

$$E(\mathbf{k}) = \frac{\hbar^2}{2}\left(\frac{\mathbf{k}^2_{\text{long}}}{m_{hh}^{*\,\text{long}}} + \frac{\mathbf{k}^2_{\text{tran}}}{m_{hh}^{*\,\text{tran}}}\right). \qquad [3]$$

The energy dispersion relation for light holes (lh) in the Γ-valley are treated within the parabolic isotropic bandstructure model given by:

$$E(\mathbf{k}) = \frac{\hbar^2\mathbf{k}^2}{2m^*_{lh}} \qquad [4]$$

where m^*_{lh} is the effective LH mass.

The both previous analytical bandstructure models, isotropic and anisotropic, assume the parabolic dispersion energy approximation which is valid for carrier kinetic energy close to the band or the valley minimum. The parabolic dispersion energy approximation might be extended to larger carrier kinetic energies by using a non-parabolic dispersion energy approximation by modifying the relation (4) as:

$$E(\mathbf{k})[1 + \alpha E(\mathbf{k})] = \frac{\hbar^2\mathbf{k}^2}{2m^*_i} \qquad [5]$$

where, for $i = e$, m^*_e is the effective electron mass, for $i = hh$, m^*_{hh} is the effective HH mass when the hole is in the HH band, and, for $i = lh$, m^*_{lh} is the effective LH mass when the hole is in the LH band. Non-parabolic bandstructure model is frequently used for electrons in III–V semiconductors, Si, and Ge due to their generally lighter effective masses. However, this approach has less applicability for holes because of their generally heavier effective masses.

In Ge, the conduction band minimum is at L-valley and the valence band minimum is at $\mathbf{k} = 0$ called Γ-valley[34] as illustrated in Fig. 2. The absolute minima of the conduction band in Ge lies along the ⟨111⟩ directions at the L-valleys, so there are four equivalent ellipsoidal valleys. Owing to their proximity in energy, the upper six equivalent ellipsoidal X-valleys along the ⟨100⟩ directions and subsequent one spherical Γ-valley at the centre of the Brillouin zone can be populated by electrons at high electric fields. The two (the HH band and the LH band) of the valence bands located at the Γ-valley are degenerate,[35] while the third one is split off by the spin-orbit interaction. The split-off band is separated from the valence band minimum at Γ-valley by the split off energy E_{SO}, as shown in Fig. 2. The split-off band is usually neglected due to its separation of energy and small density of states which play a negligible role in hole transport within semiconductors.[36] Therefore, we consider, for further simplification, only the remaining heavy and LH bands.[4] A bandgap of Ge is $E_G = 0.66$ eV at 300 K. All essential material parameters for electron and hole transport in bulk germanium in our MC simulations, including band structure coefficients, energy gap, density and mobility parameters, etc.., are summarized in Table I.

Transition Probability

The transition probability of a carrier between its states in the scattering theory can be derived from the first order time-dependent perturbation theory.[31] The transition probability between two eigenstates is the solution of Schrödinger wave equation for the perturbation potential $\mathcal{H}'$ with the unperturbed Hamiltonian operator $\mathcal{H}_{\mathcal{O}}$. In order to obtain the transition probability $S(\mathbf{k}, \mathbf{k}')$, the Schrödinger equation to be solved assumes that carriers (electrons or holes) interact with a perturbation potential $\mathcal{H}'$ and that the perturbation of the order of λ is small ($\lambda < 1$). The transition probability of an electron/hole from its initial state $\mathbf{k}$ into a final state $\mathbf{k}'$ caused by a potential due to the perturbation Hamiltonian $\mathcal{H}'$ is then given by *Fermi Golden Rule* as[45]

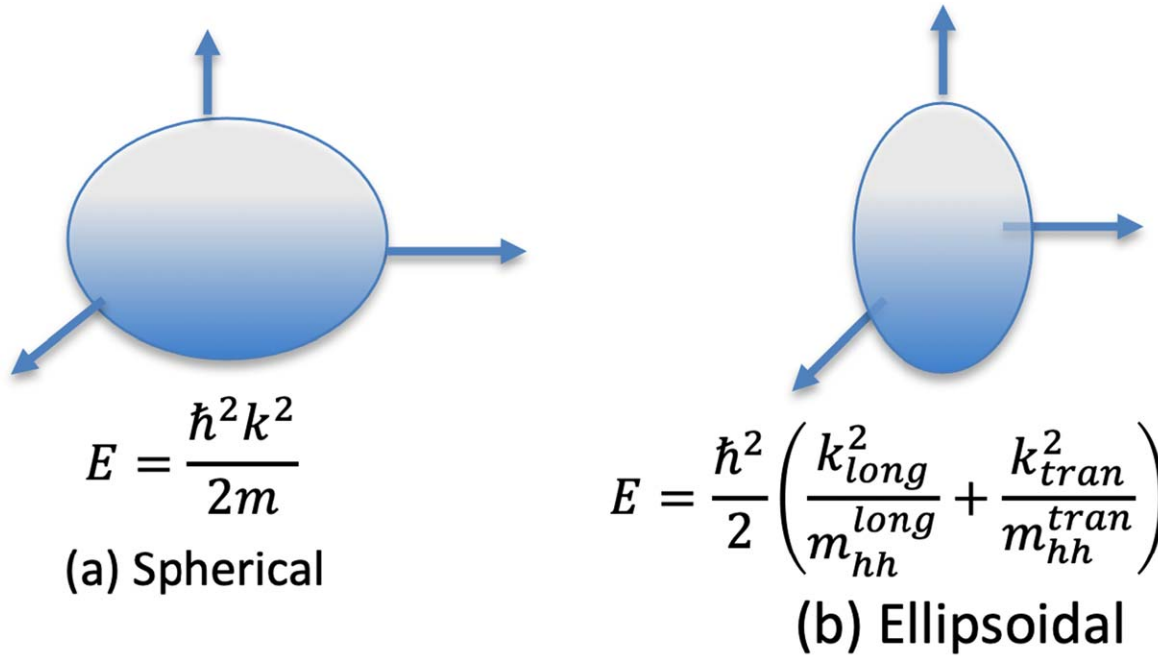

Figure 1. Spherical and ellipsoidal shapes of the surfaces of constant energy for electrons and holes in a cubic semiconductor close to the energy minima.[4]

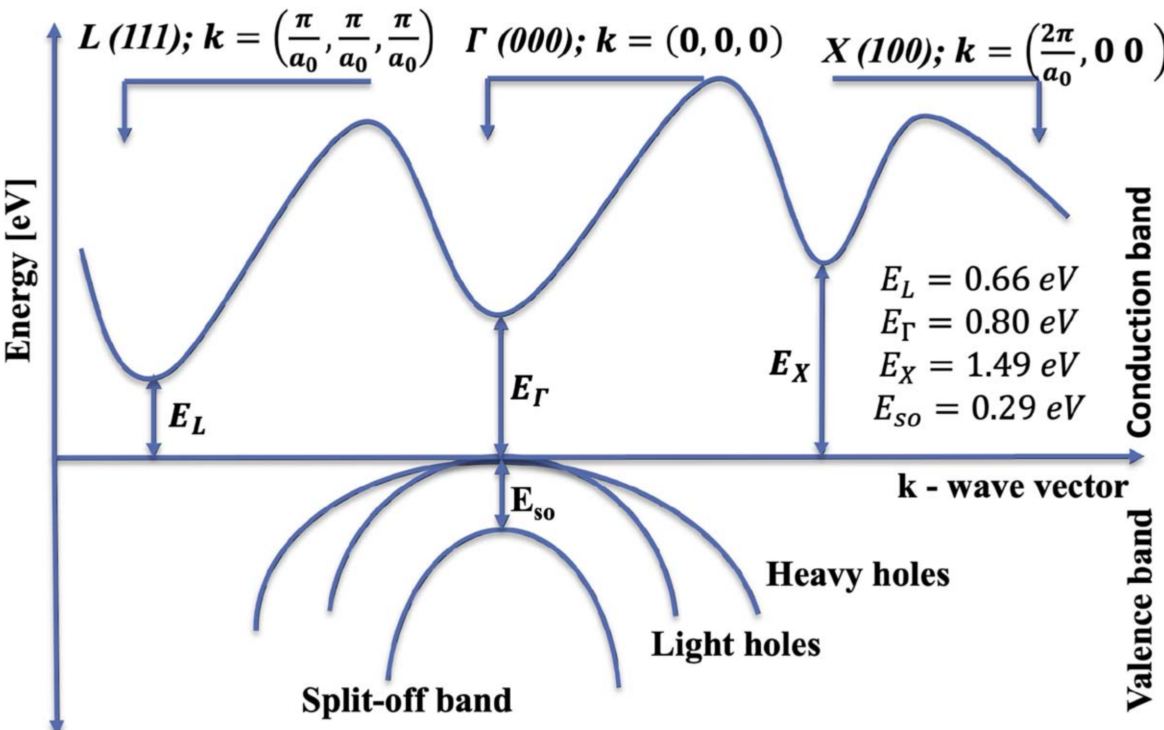

Figure 2. Bandstructure of a cubic-lattice semiconductor.

$$S(\mathbf{k}, \mathbf{k}') = \frac{2\pi}{\hbar} |\langle \mathbf{k}' | \mathcal{H}' | \mathbf{k} \rangle|^2 \delta(E(\mathbf{k}') - E(\mathbf{k}) \mp \hbar\omega). \qquad [6]$$

Equation 6 is a basic result of scattering theory, which we will apply to the scattering calculation of carriers in semiconductors. The probability $S(\mathbf{k}, \mathbf{k}')$ is derived to the first order of perturbation theory and is energy-dependent. In the particular case of a carrier-phonon interaction, when the upper sign is selected then $E'_{\mathbf{k}} = E_{\mathbf{k}} - \hbar\omega$; an energy $\hbar\omega$ of a phonon is *emitted*. If the lower sign is selected, then $E_{\mathbf{k}'} = E_{\mathbf{k}} + \hbar\omega$; an energy $\hbar\omega$ of a phonon is *absorbed*. After integrating $S(\mathbf{k}, \mathbf{k}')$, given by Eq. 6 with respect to a final state $\mathbf{k}'$, we obtain the scattering rate $\Gamma(\mathbf{k})$ as a function of the initial state $\mathbf{k}$[31,46]

$$\Gamma(\mathbf{k}) = \frac{\Omega}{(2\pi)^3} \int S(\mathbf{k}, \mathbf{k}') d\mathbf{k}', \qquad [7]$$

When we substitute Fermi Golden Rule 6 into Eq. 7, the scattering rate for the initial state $\mathbf{k}$ is given by:[47]

Table I. Material parameters of germanium for the analytical calculation of its conduction and valence bands as used within the MC simulations. The subscript r in $m_c^{r*\ \text{long}} = m_c^{*\text{long}}/m_0$ denotes the relative effective mass of a carrier c, where $c = e$ for an electron, $c = hh$ for a heavy hole, and $c = lh$ for a LH, and m_0 is the mass of electron in vacuum. The MC simulation was performed at 300 K (room temperature).

Energy gap [eV]		0.664[37]
Relative permittivity		16[37,38]
Mobility [cm^2/V-s]		3900 (electron); 1900 (hole)[39,40]
Density [g/cm^3]		5.3267[4,37]
Velocity of sound [m/s]		$v_l = 5130$, $v_t = 5360$ [4,37]
Conduction band electron valleys energy separation		
L-to-Γ valley [eV]	$\Delta_{L-\Gamma}$	0.135[4,41]
L-to-X valley [eV]	Δ_{L-X}	0.83[4,41]
Γ-to-X valley [eV]	$\Delta_{\Gamma-X}$	0.695[4,41]
Valence band hole bands energy separation		
heavy hole-to-LH band [eV]	$\Delta_{\text{hh}-\text{lh}}$	0.1 [this work]
Conduction band (non-parabolic anisotropic) electron effective mass		
L-valley (anisotropic):	$m_e^{r*\ \text{long}}$	1.588 [this work]
	$m_e^{r*\ \text{tran}}$	0.082[40]
Γ-valley (isotropic):	m_e^{r*}	0.037[42]
X-valley (anisotropic):	$m_e^{r*\ \text{long}}$	1.353[40,43]
	$m_e^{r*\ \text{tran}}$	0.288[40,43]
Conduction band (non-parabolic anisotropic) non-parabolicity coefficient		
L-valley (isotropic):	α	0.3[4]
X-valley (isotropic):	α	0.3[4]
Γ-valley (isotropic):	α	0.3[4]
Valence band (parabolic anisotropic/isotropic) hole effective mass		
Heavy hole (hh) (anisotropic):	$m_{hh}^{r*\ \text{long}}$	1.64 [this work]
	$m_{hh}^{r*\ \text{tran}}$	0.052 [this work]
Light hole (lh) (isotropic):	m_{lh}^{r*}	0.044[40,44]

Note. Note: References are mentioned in the Table.

$$\Gamma(\mathbf{k}) = \frac{2\pi}{\hbar}\frac{\Omega}{(2\pi)^3}\int|\langle\mathbf{k}'|\mathcal{H}'|\mathbf{k}\rangle|^2\delta(E(\mathbf{k}') - E(\mathbf{k}) \mp \hbar\omega)d\mathbf{k}', \quad [8]$$

Scattering Processes

MC simulations of carrier transport in semiconductors include carrier scattering mechanisms with acoustic phonons, non-polar optical phonons, and ionised impurities. The electron scattering with acoustic phonons and non-polar optical phonons might include intra-valley, where both the initial state and final state of the electron are in the same valley, or inter-valley transitions, where the final state lies in a valley different from that of the initial state.[48] The hole scattering with phonons might include intra-band transitions, where both the initial state and final state of the hole lie in the same band, or inter-band transitions, where the final state is in a band different from that of the initial state.[3,4]

The ensemble MC simulations will largely benefit from the scattering rates being prepared as a function of initial kinetic energy. These initial energy-dependent scattering rates can be quickly used to obtain the required probabilities of scattering events, as the kinetic energy of each of the particles is readily available. Therefore, in what follows, we derive this type of scattering rates.[49]

The major electron and hole scattering processes in Ge involves interactions with acoustic and non-polar optical phonons.[4] We therefore review approximations involved in the calculations of scattering rates of electrons and holes with phonons in general and then focus on the interactions with acoustic and non-polar optical phonons.[25] These electron and hole scattering rates are needed to be expressed as a function of hole initial kinetic energy to calculate the total electron and hole scattering rates including the self-scattering[4] for the ensemble MC simulations.[46] The total scattering rate serves as a principal quantity to select a scattering mechanism after the end of free flight of an electron or a hole.

Electron intra-valley and hole intra-band scattering: acoustic phonons.—The carrier scattering with phonons will be briefly overviewed in the following sections. At the end of each overview section, the generalised scattering of a carrier will be separated into the electron scattering and the hole scattering to clearly distinguish the two separate charge carriers, which might have different relevant scattering mechanisms and will inevitably have different material scattering parameters.

The probability of a carrier to scatter from an initial state $|\mathbf{k}\rangle$ to a final state $|\mathbf{k}'\rangle$ by an acoustic phonon can be further simplified by an equi-partition approximation, assuming that this scattering is elastic.[4] The elastic scattering approximation of the phonon interaction means that the carrier energy dissipated by acoustic phonon emission is equal to the carrier energy immersed by acoustic phonon absorption.

The scattering probability of a carrier to scatter from an initial state $\mathbf{k}$ to a final state $\mathbf{k}'$ in the equi-partition approximation is given by:[50]

$$\mathrm{P}(\mathbf{k}', \mathbf{k}) = \frac{\mathcal{D}_{\text{AC}}^2 k_B T_L}{4\pi^2\rho v_s^2}\iiint G^2(\mathbf{k}', \mathbf{k}) \times \delta[E(\mathbf{k}') - E(\mathbf{k})]\mathbf{k}'^2 d\mathbf{k}' d\cos(\theta)d\phi. \quad [9]$$

where D_{AC} is the deformation potential for acoustic phonons, k_B is the Boltzmann constant, ρ is the crystal density, v_s is the sound velocity, and T_L is the lattice temperature. The scattering probability per unit time, $\Gamma[E(\mathbf{k})]$, for absorption and emission processes in the equi-partition approximation can be obtained after integrating over all possible final states. The term $G(\mathbf{k}', \mathbf{k})$ is called the overlap integral, which consist of the $\mathbf{k}$ and $\mathbf{k}'$ states involved in carrier transport. The overlap integral depends on the symmetry of the electron/valence band wavefunctions (s-type or p-type) and on the specific atomic orbitals and their spatial arrangement, but simple wavefunction approximations give $G(\mathbf{k}', \mathbf{k}) = 1/2$ for electron intra-valley and intra-valley, as well as for hole intra-band and inter-band transitions.

If a non-parabolic energy dispersion relation (5) is required for electrons with a lighter effective mass, an electron scattering rate for its interaction with the acoustic potential of phonons is given by:

$$\Gamma[E(\mathbf{k})] = \frac{\sqrt{2}\ \mathcal{D}_{\text{AC}}^2 k_B T_L\ (m_e^*)^{3/2}}{\pi\rho\ v_s^2\ \hbar^4} \times \sqrt{E(\mathbf{k})(1 + \alpha E(\mathbf{k}))}\ (1 + 2\alpha E(\mathbf{k})). \quad [10]$$

where m_e^* is the electron effective mass, α is the electron non-parabolicity coefficient (see Table I), and $\hbar$ is the reduced Planck constant.

If we use the parabolic energy dispersion relation 1 in the expression for the scattering rate (8), we can write a hole acoustic scattering rate as:[4,51]

$$\Gamma[E(\mathbf{k})] = \frac{\sqrt{2}\ \mathcal{D}_{\mathrm{AC}}^2\, k_B T_L (m_i^*)^{3/2}}{\pi\rho\ v_s^2\ \hbar^4}\sqrt{E(\mathbf{k})}, \quad [11]$$

where the hole effective mass will be for a LH band if $i = lh$, and for a HH band if $i = hh$.[52]

Electron intra-valley/inter-valley and hole intra-band/inter-band scattering—non-polar optical phonons.—Carrier scattering due to non-polar optical phonons can be treated similarly to the acoustic deformation potential scattering as described in Eq. 9. We consider the non-polar optical scattering of carriers by a combination of longitudinal optical (LO) and transverse optical (TO) modes, assuming common frequency for both. Therefore. one can use a deformation potential constant $\mathcal{D}_{op}^2$, which represents an average over optical strains in all directions.[53] As in the case of the acoustic scattering, the only angular dependence in the non-polar optical scattering rate is that due to the overlap integral $G(k'k)$, which reduces the total rate for both intra- and inter-band scattering by a factor of 2. Hence, the electron scattering rate for the non-polar optical phonons for intra-valley transitions with the consideration of non-parabolic energy dispersion relation 5 reads:

$$\Gamma(E) = \frac{Z\mathcal{D}_{op,i\to i}^2 (m_e^*)^{3/2}}{\sqrt{2}\,\pi\rho\ \omega_{op}\ \hbar^3}\left[\begin{pmatrix} N_q \\ N_q + 1\end{pmatrix}\right] \times \sqrt{E'(1+\alpha E')}\ (1 + 2\alpha E'), \quad [12]$$

where Z is the number of equivalent valleys. The terms N_q and $N_q + 1$ are the occupation numbers of the lattice state $|N_q\rangle$ given by the Bose-Einstein distribution, which represent absorption (the upper symbol N_q) and emission (the lower symbol $N_q + 1$) of a single phonon of energy $\hbar\omega_{op}$. The Bose-Einstein phonon distribution function (N_q) is defined as:

$$N_q = \frac{1}{\exp\left(\frac{\hbar\omega_{op}}{k_B T}\right) - 1}. \quad [13]$$

The final energy E' in the electron scattering rate (12) is given by:

$$E' = E \pm \hbar\omega_{op}. \quad [14]$$

The electron scattering rate for the non-polar optical phonons for inter-valley transitions with the consideration of non-parabolic energy dispersion relation 5 is:

$$\Gamma(E) = \frac{Z_{ij}\mathcal{D}_{op,i\to j}^2 (m_e^*)^{3/2}}{\sqrt{2}\,\pi\rho\ \omega_{ij}\ \hbar^3}\left[\begin{pmatrix} N_q \\ N_q + 1\end{pmatrix}\right] \times \sqrt{E'(1+\alpha E')}\ (1 + 2\alpha E'), \quad [15]$$

where Z_{ij} is the number of equivalent valleys and ω_{ij} is the non-polar optical frequency for inter-valley phonons. The final energy E' in the electron scattering rate (15) is now given as:

$$E' = E \pm \hbar\omega_{ij} - \Delta V_{ij}. \quad [16]$$

The hole scattering rate for the non-polar optical phonons considering intra-band transitions (transition occurred between the HH band to the HH band, and also between the LH band to the LH band), in the spherical and isotropic band approximation model, is given by:

$$\Gamma[E(\mathbf{k})] = \frac{\mathcal{D}_{op,i\to i}^2 (m^*_i)^{\frac{3}{2}}}{\sqrt{2}\,\pi\hbar^3\rho\ \omega_{op}}\left[\begin{pmatrix} N_q \\ N_q + 1\end{pmatrix}\right]\sqrt{E'(\mathbf{k})}, \quad [17]$$

where $i = hh$ stands for the HH band and $i = lh$ stands for the LH band. The deformation potential constant $D_{op,i\to i}^2$ is for intra-band transitions between two identical bands, either the HH ($i = hh$) or the LH ($i = lh$). The final energy E' in the hole scattering rate (17) is given by the expression (14), where ω_{op} is the non-polar optical frequency for holes interacting with intra-band phonons.

The hole scattering rate in the spherical and isotropic band approximation model for inter-band transitions (transition occurred between the HH band to the LH band, and also between the LH band to the HH band) due to the non-polar optical phonons considering is given by:

$$\Gamma[E(\mathbf{k})] = \frac{\mathcal{D}_{op,i\to j}^2 (m_i^*)^{\frac{3}{2}}}{\sqrt{2}\,\pi\hbar^3\rho\ \omega_{ij}}\left[\begin{pmatrix} N_q \\ N_q + 1\end{pmatrix}\right]\sqrt{E'(\mathbf{k})}, \quad [18]$$

where the suffix of the effective mass term $i = hh$ stands for the HH band and $i = lh$ stands for the LH band. The deformation potential constant $\mathcal{D}_{op,i\to j}^2$ is for inter-band transitions between two different bands, from the HH band ($i = hh$) to the LH band ($j = lh$) or from the LH band ($i = lh$) to the HH band ($j = hh$). ω_{ij} is the non-polar optical frequency for holes interacting with inter-band phonons.

Deformation potentials and phonon energies for the interactions of electrons and holes with acoustic and non-optical phonons in Ge are listed in Table II for intra-band and inter-band transitions, respectively. Finally, the hole intra-band and inter-band optical transitions between HH and LH are summarised in Table III.

Ionized impurity scattering.—In a doped semiconductor, an electron or a hole interacts with the Coulomb potential of a ionized impurity atom, which is the source of scattering charge. In general, the carrier (electron or hole) scattering on ionized impurities is an elastic scattering process. Since the carrier is not alone in the semiconductor but is surrounded by many other carriers in a many-body system, the carrier interaction via Coloumb potential is affected by these other carriers.[55,56]

In what follows, we summarise the most frequently used models for carrier scattering with ionised impurities which are Conwell-Weisskopf[57] ionised impurity scattering model and Brooks-Herring[58] ionised impurity scattering model. These two models will be briefly overviewed, and the notorious divergence present in the Brooks-Herring model will be resolved by the Third Body Exclusion model.[46,59]

Conwell-Weisskopf ionised impurity scattering model.—The Conwell-Weisskopf ionised impurity scattering model (CW) does not need to consider a screening of Coulomb interaction among charges (free or fixed) and assumes a bare Coulomb potential in the form:[57,60]

$$v_r = \frac{e^2}{4\pi\kappa r} \quad [19]$$

However, the formula for calculating the carrier relaxation time for scattering with ionised impurities would diverge for $\mathbf{q} = 0$. Therefore, the model excludes scattering at very small angles, which is physically justified assuming that a carrier would always scatter with the closest ionised impurity if the concentration of ionised impurities is N_i. A minimum angle of scattering (α) is obtained using Rutherford theory of impact parameter (b) given by:[45]

$$b = \frac{e^2}{8\pi\kappa E}\coth(\alpha/2). \quad [20]$$

The maximum of the impact parameter ($b_{\max}$) when the impact ionisation scattering becomes operative is approximated by a half distance between ionised impurity scattering centres as:

Table II. Phonon deformation potentials and energies used in the electron and hole MC simulations of Ge. HH stands for heavy hole, and LH for light hole. Note: References to material parameters from literature are also included while parameters exclusive to this work are marked with a symbol "[a]".

Electron intra-valley scattering:	*L*-Valley	Γ-Valley	*X*-Valley
Deformation potential: Acoustic phonons [eV]	9.0 [a]	5.0[4]	9.0[4]
Deformation potential: Optical non-polar phonons [eV/cm]	2.7×10^8 [a]	—	—
Phonon energy: Optical non-polar phonons [eV]	0.03704[5]	—	—
Electron inter-valley scattering:	***L*-to-*L*-Valley**	***L*-to-Γ-Valley**	***L*-to-*X*-Valley**
Deformation potential: Optical non-polar phonons [eV/cm]	3.0×10^8 [4]	2.0×10^8 [4]	4.06×10^8 [4]
Phonon energy: Optical non-polar phonons [eV]	0.03704[4,5]	0.0276[4]	0.0276[4]
Electron inter-valley scattering:	**Γ-to-*X*-Valley**	***X*-to-*X*-Valley**	—
Deformation potential: Optical non-polar phonons [eV/cm]	1.0×10^9 [4]	8.0×10^8 [4]	—
Phonon energy: Optical non-polar phonons [eV]	0.0276[4]	0.025[4]	—
Hole intra-band scattering:	**HH Band**	**LH Band**	—
Deformation potential: Acoustic phonons [eV]	6.0 [a]	4.6 [a]	—
Deformation potential: Optical non-polar phonons [eV/cm]	9.0×10^8 [54]	9.0×10^8 [54]	—
Phonon energy: Optical non-polar phonons [eV]	0.037[4,5]	0.037[4,5]	—
Hole inter-band scattering:	**HH-to-LH**	**LH-to-HH**	
Deformation potential: Optical non-polar phonons [eV/cm]	9.0×10^8 [54]	9.0×10^8 [54]	—
Phonon energy: Optical non-polar phonons [eV]	0.037[4,5]	0.037[4,5]	—

$$b_{\max} = \frac{1}{2} N_i^{-1/3}. \quad [21]$$

The electron scattering with ionised impurities uses the non-parabolic energy dispersion (5). The electron Conwell-Weisskopf scattering rate for ionised impurities in the non-parabolic approximation is therefore given in its energy form by:[4]

$$\Gamma^{\mathrm{CW}}(E) = \frac{\sqrt{2} N_i b_{\max}^2}{(m_0 m_e^*)^{1/2}} \frac{E^2(1 + \alpha E)}{[E(1 + \alpha E)]^{3/2}} \quad [22]$$

where m_e^* for the effective electron mass given by average of the effective longitudinal electron mass ($m_{e,\,\mathrm{long}}^*$) and the effective transverse mass ($m_{e,\,\mathrm{tran}}^*$) as:

$$m_e^* = [m_{e,\,\mathrm{long}}^* \times (m_{e,\,\mathrm{tran}}^*)^2]^{1/3}$$

The hole scattering with ionised impurities uses a simpler parabolic energy dispersion (1). Therefore, the hole Conwell-Weisskopf scattering rate for ionised impurities in the parabolic approximation is just:

$$\Gamma^{\mathrm{CW}}(E) = \frac{\sqrt{2} N_i b_{\max}^2}{(m_0 m_i^*)^{1/2}} E^{1/2} \quad [23]$$

where $i = hh$ is again m_{hh}^* for the effective HH mass when the hole is in the HH band, and $i = lh$ is m_{lh}^* is the effective LH mass when the hole is in the LH band.

Brooks-Herring ionised impurity scattering model.—The Brooks-Herring model for ionised impurity scattering assumes an interaction of a carrier via screened Coulomb potential with single scattering centre.[61] As mentioned before, the scattering rate used in MC

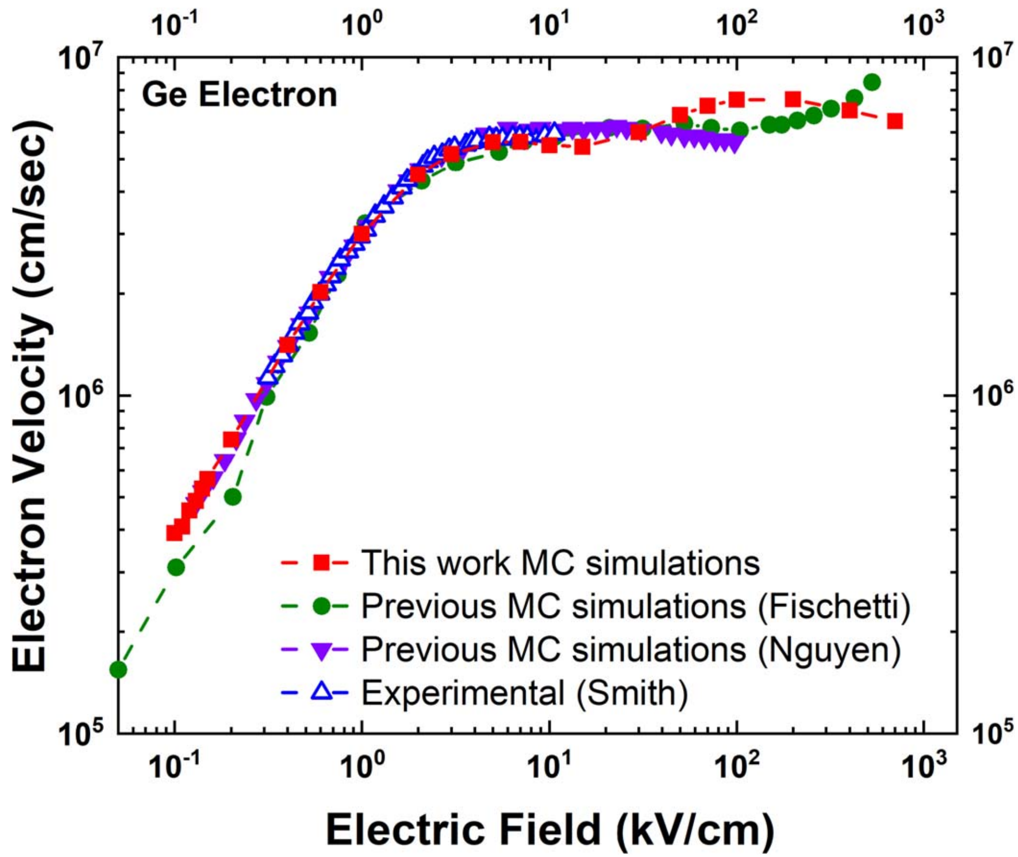

Figure 3. Average drift velocity of electrons in Ge as a function of applied electric field in the ⟨100⟩ crystallographic orientation at 300 K. This work MC simulations shown by the closed red squares are compared against experimental results[1] given by the open blue up triangles (Smith). The closed green circles (Fischetti) and closed violet down triangles (Nguyen) are the previous full-band MC simulations of Refs. 28 and 68 respectively.

Table III. Summary of transitions of holes within the heavy hole band, the light hole band, and between the heavy hole band and the light hole band in Ge.

Intra-band transitions		Inter-band transitions	
Initial state	**Final state**	**Initial state**	**Final state**
Heavy Hole	Heavy Hole	Heavy Hole	Light Hole
Light Hole	Light Hole	Light Hole	Heavy Hole

simulations for this depends on type of carrier, electron or hole, because the bandstructure model for transport of these two carriers is different. The electron scattering rate as a function of the electron initial energy E for its a non-parabolic anisotropic bandstructure model is given by:[4,46]

$$\Gamma^{\mathrm{BH}}(E) = \frac{N_i e^4}{2\pi\sqrt{2m_0 m_e^*}\,\kappa^2\,(\beta_E^2)^2}\sqrt{E(1+\alpha E)} \times \frac{1+2\alpha E}{1+4E(1+\alpha E)/\beta_E^2}, \quad [24]$$

where the Debye–Hückel inverse screening length β_E in an energy form is given by:

$$\beta_E^2 = \frac{\hbar^2}{2m_0 m_e^*}\frac{e^2 N_i}{\kappa\, k_B T}. \quad [25]$$

Note that the dielectric permittivity κ can also be expressed as $\kappa = \epsilon_0 \epsilon_S$, where ϵ_0 is the permittivity of vacuum and ϵ_S is the relative static permittivity of the material. This expression for a scattering rate uses the overlap integral equal to unity.

The hole scattering rate as a function of the hole initial energy E for its parabolic anisotropic (heavy-hole band) and isotropic (light-hole band) bandstructure model is given by:

$$\Gamma^{\mathrm{BH}}(E) = \frac{N_i e^4}{2\pi\sqrt{2m_0 m_i^*}\,\kappa^2\,(\beta_E^2)^2}\frac{\sqrt{E}}{1+4E/\beta_E^2}. \quad [26]$$

where the hole effective mass m_i^* again distinguishes between the HH band ($i = hh$) and the LH ($i = lh$) band, and β_E is the inverse screening length. Furthermore, the derivation of the inverse screening length can be approached using the Debye–Hückel and Thomas–Fermi (TF) screening models.[62–64]

The MC simulations here adopt a static screening in the random phase approximation.[65] The random phase approximation[66] considers carrier-carrier interactions but neglects effects of correlation and exchange.[63] The inverse screening length in the static screening model[42,60,67] containing the Fermi half integrals ($\mathcal{F}_{-1/2}$, $\mathcal{F}_{1/2}$) may be expressed in an energy form as:

$$\beta_E{}^2 = \frac{\hbar^2}{2m_0 m_i^*}\frac{e^2 N_i}{\kappa}\frac{\mathcal{F}_{-1/2}(\eta)}{\mathcal{F}_{1/2}(\eta)},\ \eta = \frac{1}{k_B T}(E_F - E_C - \delta E_{ij}), \quad [27]$$

where E_F is Fermi energy level, E_C is the conduction or the valence band edge, and δE_{ij} is the electron energy valley separation or the hole energy heavy-band to light-band separation if applicable. The index i in the carrier effective mass stands for the electron effective

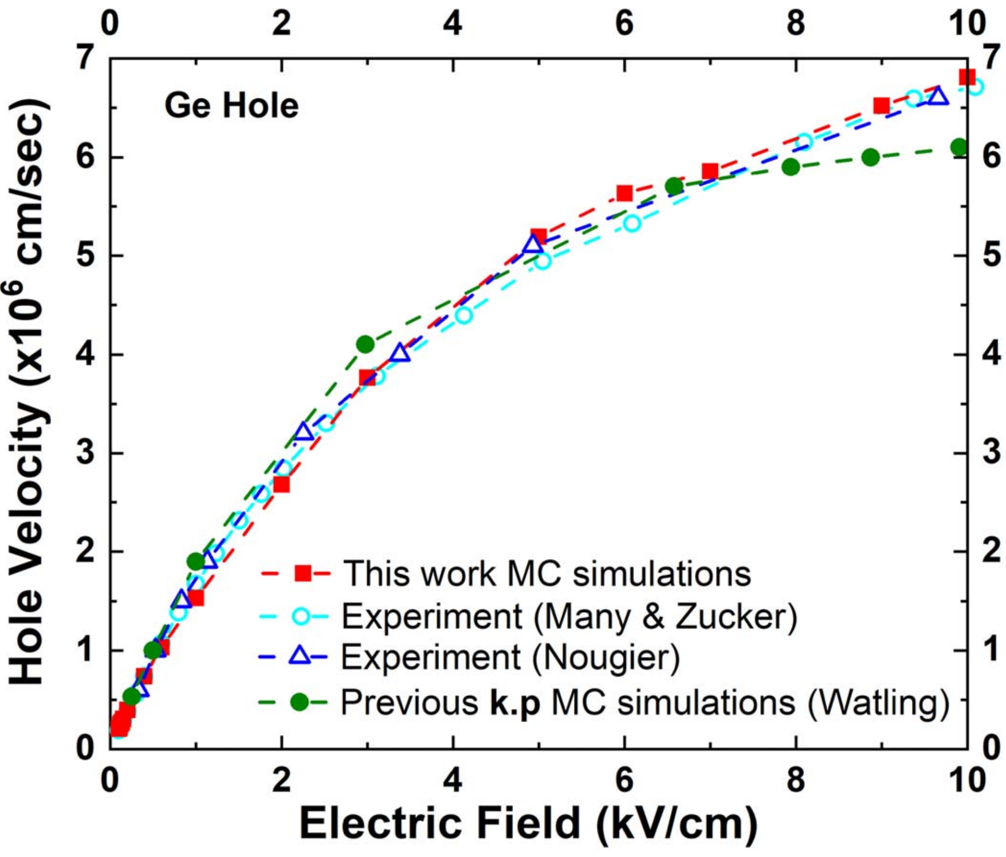

Figure 4. Average drift velocity of holes in Ge as a function of applied electric field in the ⟨100⟩ crystallographic orientation at 300 K.[3] This work MC simulations shown by the closed red squares are compared against experimental results extracted from Fig. 7 (Many & Zucker) in Ref. 69 shown by the open cyan circles and experimental results (Nougier) of Ref. 2 shown by the open blue triangles. The closed green circles (Watling) are from previous **k.p** MC simulations.[9]

mass when $i = e$, for the hole heavy-band effective mass when $i = hh$, and for the hole light-band effective mass when $i = lh$.

Our MC simulations calculate the Fermi energy level (E_F) self-consistently and, instead of the lattice temperature T, also calculate an electron temperature (T_e) from the carrier concentration (given by the ionised impurity concentration N_i) and the average kinetic energy of the carrier at each time step.[63] Therefore, the argument η of the Fermi half integrals reads:

$$\eta = \frac{1}{k_B T_e}(E_F - E_C - \delta E_{ij}).$$

Third-body exclusion.—Our MC simulations use a carrier scattering rate for the ionised impurities based on Ridley's model (third-body exclusion) to eliminate divergence in Brooks-Herring formula.[46,59]

Ridley model assumes that since the carrier scattering with individual ionised impurity has to be truly two-body nearest scattering process, we have to make sure that any interaction with another neighbour scattering centre is excluded.[46,59,63] Therefore, Brooks-Herring scattering rate Γ_{BH} is substituted into the following expression:

$$\Gamma(E) = a^{-1}v(E)\left[1 - \exp\left(-\frac{\Gamma^{\mathrm{BH}}(E)}{a^{-1}v(E)}\right)\right], \qquad [28]$$

where a is the mean length between impurity centres and can be found via the relation:

$$a = (2\pi N_i)^{-1/3}. \qquad [29]$$

$v(E)$ is the carrier drift velocity given by:

$$v(E) = \sqrt{2/m_i^*}\ \frac{\sqrt{E(1 + \alpha E)}}{1 + 2\alpha E}.$$

The carrier drift velocity is simplified to:

$$v(E) = \sqrt{2/m_i^*}\ \sqrt{E}$$

where i is index of a carrier. When $i = e$, m_i^* is the electron effective mass, when $i = hh$, m_i^* is the hole heavy-band effective mass, and $i = lh$ is the hole light-band effective mass.

Drift Velocity, Mobility, and Other Quantities from Ensemble Monte Carlo Simulations

The ensemble MC technique is employed to validate the bandstructure model and scattering mechanisms identified as essential in Ge against available experimental data and previous simulations. We would like to stress once more that the aim of this work is not to develop a highly universal transport model for all transport conditions (crystallographic orientations, temperature, strain, etc..) but to develop a fast and reliable simple transport simulation model for Ge only in the ⟨100⟩ crystallographic orientation at room temperature of T = 300 K. The validation starts with a comparison of the average electron and hole drift velocity as a function of the electric field ($v - E$) as shown in Figs. 3 and 4, respectively. The

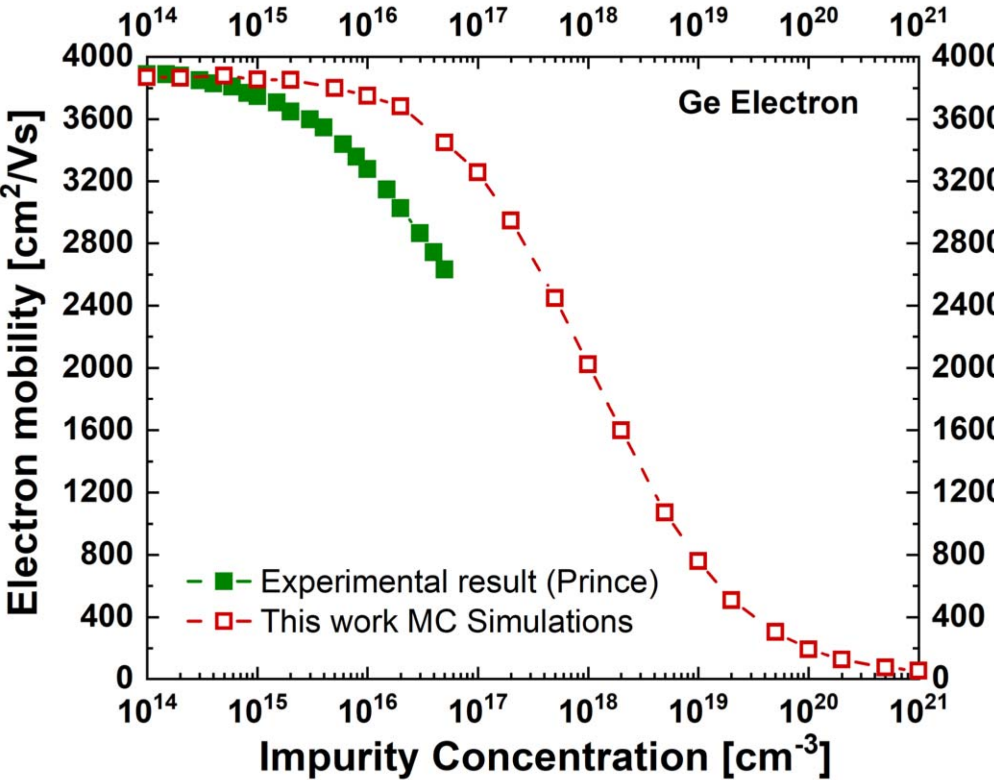

Figure 5. Mobility of electrons in Ge as a function of the impurity concentration in the ⟨100⟩ crystallographic orientation at 300 K and at a low field of 0.1 kV cm^{-1}. The open and closed circle symbols refer to simulation and experimental results,[14] respectively. The shift in the simulation data is due to not all dopants reported in experimental results being electrically active, resulting in a lower active doping concentration than reported. Note that the trend of simulation data perfectly agrees with the trend of experimental data.

electric field is varied from 0.1 to 1000 kV cm^{-1} for electrons on a logarithmic scale and from 0.1 to 10 kV cm^{-1} for holes on a linear scale. The orientation of the electric field is chosen to be parallel to the ⟨100⟩ crystallographic orientation. The electron transport simulations assume anisotropic and non-parabolic *L*-valleys, which are the lowest valleys in the conduction band, an isotropic and non-parabolic Γ-valley, which is the second valley, and anisotropic and non-parabolic *X*-valleys, which are the third valleys. The hole transport simulations assume the anisotropy and parabolicity at the Γ-valley of the valence band for the heavy-hole band and the anisotropy and parabolicity at Γ-valley for the light-hole band. The MC simulated electron and hole drift velocity versus applied electric field are in very good agreement with the experimental results for electrons[1] and for holes.[2,69] Figure 3 shows that the electron drift velocity steadily increases at relatively low applied electric fields when the increasing field progressively accelerates electrons. The electrons at these low electric fields will interact mostly with acoustic phonons. As the applied electric field increases, the electrons will acquire larger kinetic energies and start to interact with non-polar optical phonons. With further increase of electron kinetic energy, the electrons might undergo transitions from the lowest conduction *L*-valley to upper *X*- and Γ-valleys. Our MC simulated electron drift velocity is nearly identical to experimental data and agrees well with the previous full-band MC simulations up to electric field of 40 kV cm^{-1} at which point our simulations start to slightly overestimate previous full-band MC simulations. However, since no experimental data are available for these high electric fields, a definitive conclusion is not possible at the moment. Our simulated results of hole $v - E$ characteristics are in excellent agreement, if not better than, the previous **k.p** MC simulation[9] as demonstrated in Fig. 4.

At low electric fields, the hole velocity increases linearly with the increase of electric field as the holes are accelerated by the field and because the holes in an chiefly elastic scattering system are not losing significant amounts of energy. At high electric field, electrons lose more energy due to the increased inelastic scattering with non-polar optical phonons. Hence, the hole velocity at high electric field will start to saturate. At very high electric fields, the full band **k.p** MC simulations start to underestimate the experimental data while our MC simulations are closely following the trend of the experimental data. This excellent agreement with experiments is attributed to the use of significantly anisotropic hole effective mass in the heavy band. The longitudinal HH effective mass is quite heavy ($1.64m_0$) while the transverse HH effective mass is relatively low ($0.052m_0$). The low transverse HH effective mass helps holes move faster as one would expect from the large longitudinal HH effective mass keeping this excellent agreement with experiment. The transitions of holes from the HH band to the LH band with an isotropic, single LH effective mass ($0.044m_0$) also assist the hole at the very high electric fields to achieve a larger average hole drift velocity.

Figure 5 presents the electron mobility as a function of the ionised impurity concentration in bulk Ge at a very low electric field of 0.1 kV cm^{-1}. The impurities concentrations vary from 1×10^{14} cm^{-3} to 1×10^{21} cm^{-3}. The mobility is the largest at a low doping concentration and begins to decline as the doping concentration increases because of increasing interactions of carriers with ionised impurities. Note that the scattering with ionised impurities is elastic and thus will not reduce the kinetic energy of carriers but will randomise their movement (drift) under applied electric field. Electron mobility decreases with increasing doping concentration but tends to saturate at very high doping levels due to the enhanced screening effect. This will be explained in detail for hole mobility in the following paragraph. Finally, the apparent shift of the simulated electron mobility when compared to experimental data[14] is caused by the fact that the reported *n*-type doping concentration in the experiment assumes that all the dopants are activated, with the dopant activation at 100%. However, not all *n*-type dopants are

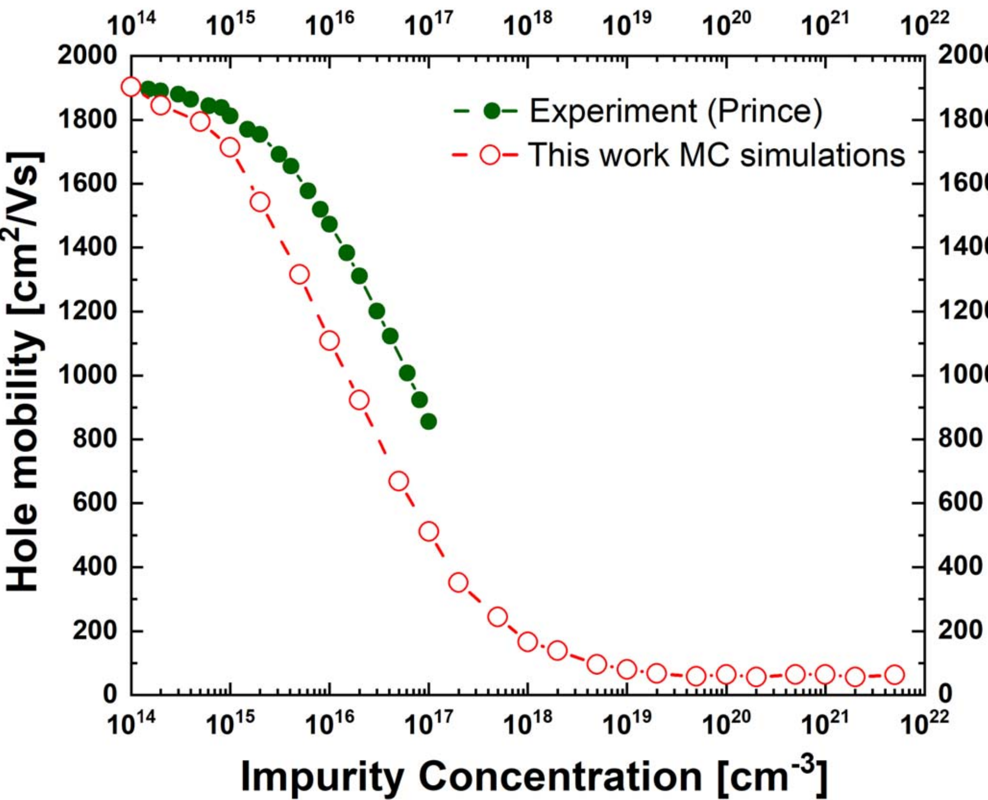

Figure 6. Mobility of holes in Ge as a function of the impurity concentration in the ⟨100⟩ crystallographic orientation at 300 K and at a low field of 0.1 kV cm^{-1}. The open and closed circle symbols refer to simulation and experimental results,[14] respectively. The shift in the simulation data is again because not all dopants in experimental results are activated and the active doping concentration is lower than the one reported. Note that the trend of simulation data perfectly agrees with the trend of experimental data.

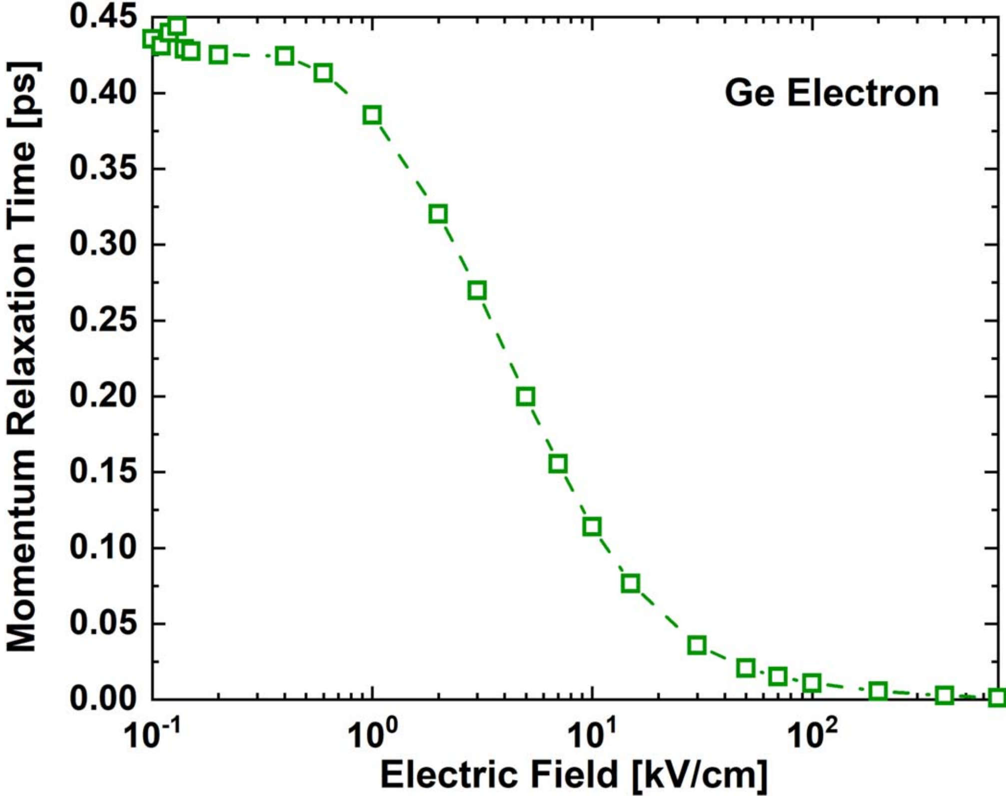

Figure 7. The momentum relaxation time of electrons in Ge as a function of the electric field at 300 K.

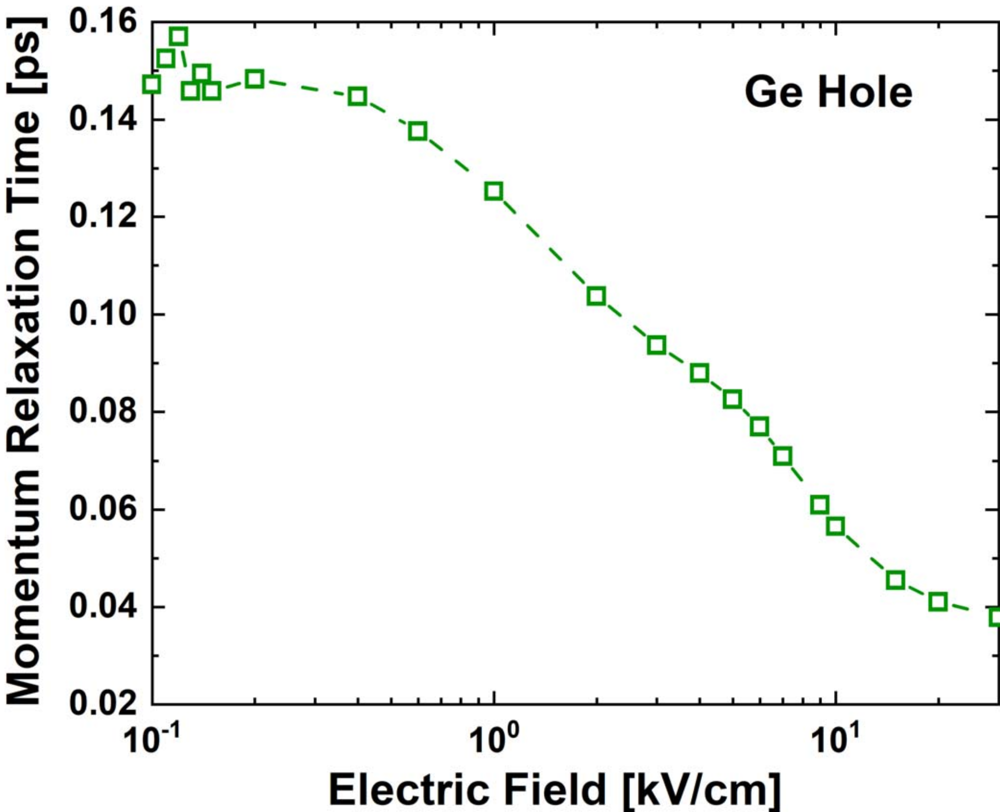

Figure 8. The momentum relaxation time of holes in Ge as a function of the electric field at 300 K.

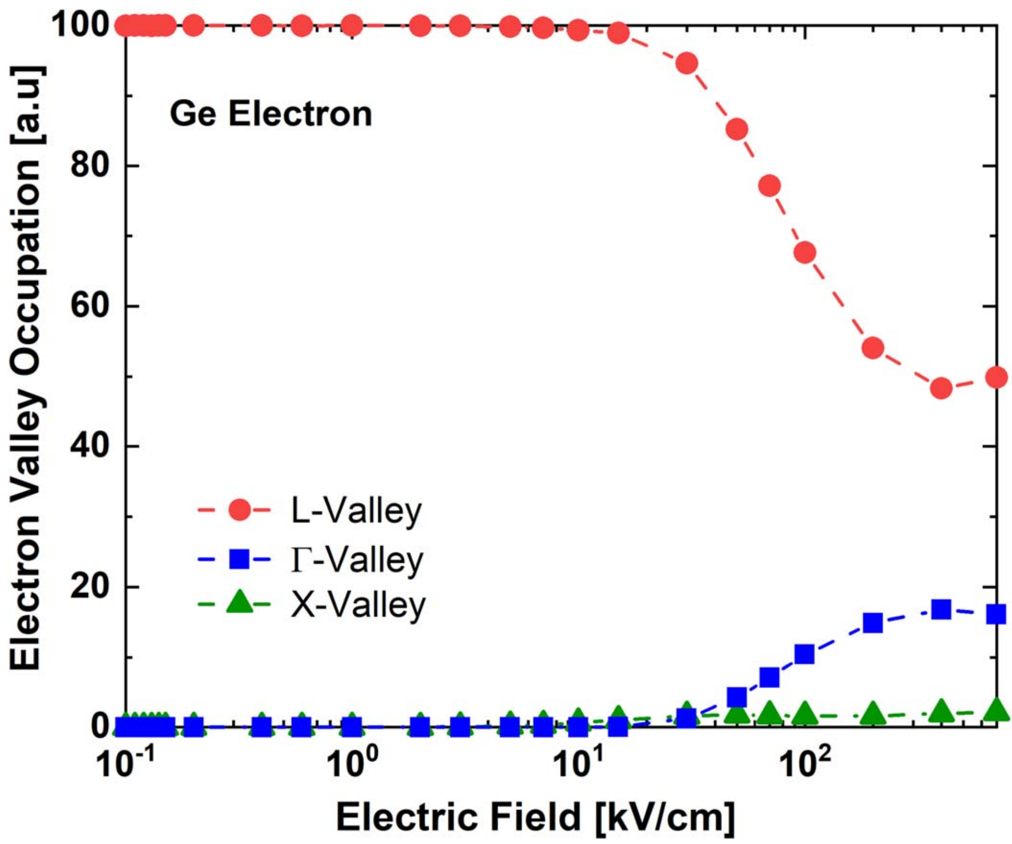

Figure 9. The electron valley occupation of the conduction band in bulk Ge as a function of the electric field at 300 K.

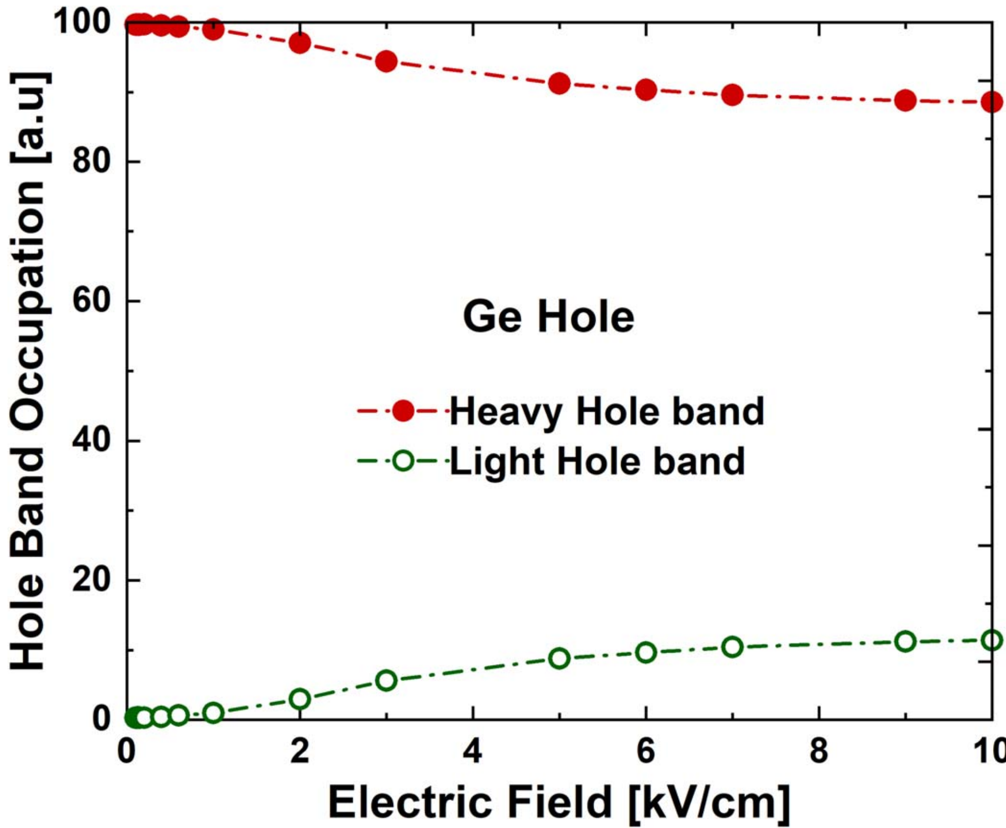

Figure 10. The hole occupation of the heavy-hole and light-hole bands of the valence band in bulk Ge as a function of the electric field at 300 K.

activated. Therefore, for example, the simulation results for the electron mobility at a doping concentration of 1×10^{11} cm^{-3} are equivalent to the active dopant concentration at 1×10^{15} cm^{-3}.

Figure 6 shows the hole mobility, again, as a function of the ionised impurity concentration in bulk Ge at the same, very low electric field of 0.1 kV cm^{-1}. The impurities concentrations vary from 1×10^{14} cm^{-3} to 1×10^{20} cm^{-3}. Similarly to the experimental data for holes, there is apparent shift of the simulated hole mobility compared to the experimental data.[14] This shift is also caused by the fact that the reported p-type doping in the experiment assumes that all the dopants are activated. Therefore, for example, the results for the hole mobility at a doping concentration of 2×10^{16} cm^{-3} are equivalent to the active dopant concentration at 8×10^{15} cm^{-3}.

We observe from Fig. 6 that the hole mobility is modestly reduced at very low ionized impurity concentrations, as expected, because of a weak hole screening at these low hole concentrations. When the low hole concentration increases above 2×10^{15} cm^{-3} then the mobility starts to significantly decline as the concentration increases. According to Eq. 25, the inverse screening length decreases with the increased impurity concentration. With the decreasing of screening length, the scattering rate increases until the ionised impurity concentration becomes high (1×10^{19} cm^{-3}), at which it starts to decrease. The MC simulation trend of mobility of holes in Ge is in a good agreement with the experimental result at 300K as shown in Fig. 6.

Figures 7 and 8 show the momentum relaxation time for electrons and holes, respectively, as a function of the electric field in bulk Ge at lattice temperature T = 300 K. We observe that the carrier relaxation time is large at a low electric field, and then exponentially decreases with the increasing electric field corresponding to a field higher than 50×10^3 V/cm, which is a negative differential resistance (NDR) region due to intervalley scattering to higher Γ and L valleys. Moreover, the decrease in the momentum relaxation time is caused by loss of momentum due to interactions with acoustic and non-polar optical phonons (electrons or holes scatter more frequently and relax more momentum). However, the momentum relaxation mechanisms are acoustic phonon scattering at lower electric field, but non-polar optical phonon and inter-valley scatterings are the dominant momentum relaxation mechanisms when the electric field becomes higher.

At an electric field of 7 kV cm^{-1}, negative differential resistance (NDR) occurs in the electron drift velocity due to an increase in phonon emission. While electrons still remain in the L-valley, increased scattering with non-polar optical phonons results in a decline in the drift velocity despite acquiring greater kinetic energy from the increasing electric field. As shown in Fig. 9, L-valley occupation remains near 100% at and beyond this field. When the field reaches 30 kV cm^{-1}, electrons begin transitioning to the Γ-valley, where their lower effective mass leads to a renewed increase in drift velocity. Transitions to the X-valley remain negligible and do not contribute significantly to drift velocity.

The occupation of three lowest valleys in the conduction band considered for the transport simulations of electrons is plotted in Fig. 9 as a function of applied electric field at room temperature (T = 300 K). The lowest L-valley will be substantially occupied until about an electric field of 20 kV cm^{-1}, when more frequent transitions of electrons from the L-valley to the Γ-valley will increase its occupation up to 18%. While there will be electrons with large kinetic energies reaching the X-valley, its occupation will remain quite low, at about 2%.

Figure 10 shows the occupation for the HH and LH bands as a function of the electric field in MC simulations of hole transport in germanium at room temperature. At the beginning of an MC simulation, all holes are assumed to occupy the HH band, resulting in 100% occupation. This is because, at thermal equilibrium and low electric fields, the HH band lies lower in energy (and has a higher effective density of states) compared to the LH band, making it the energetically favourable state for hole occupation. As the electric field increases beyond approximately 0.5 kV cm^{-1}, the holes gain sufficient kinetic energy, and the non-equilibrium carrier distribution

leads to band repopulation. This results in the transfer of holes from the HH band to the LH band due to interband non-polar phonon scattering.

In other words, high energy carriers can overcome the band splitting, leading to interband non-polar phonon scattering. This is evident in the band occupations shown in the figure, where the LH band population increases. However, despite the increase in phonon-mediated interband scattering, hole transport remains dominated by holes in the HH band with a larger hole effective mass and hole density of states.

Conclusions

We have developed a highly efficient and fast transport model for electrons and holes in Ge using ensemble MC simulations. While this transport model is valid only for Ge electron and hole transport in the $\langle 100 \rangle$ crystallographic orientation at room temperature (T = 300 K), it accurately reproduces experimental data. The electron transport model employs an analytical bandstructure with highly anisotropic (ellipsoidal) non-parabolic L- and X-valleys. The longitudinal electron effective mass of the L-valley is $1.588m_0$, and the transverse electron effective mass is $0.082m_0$. For the X-valley, the longitudinal electron effective mass is $1.353m_0$, and the transverse effective mass is $0.288m_0$. The Γ-valley is described by an isotropic non-parabolic model using an effective electron mass of $0.037m_0$. The hole transport model also uses an analytical bandstructure with a highly anisotropic (ellipsoidal) parabolic HH band. The longitudinal HH effective mass is large at $1.64m_0$, while the transverse HH effective mass is small at $0.052m_0$. The LH band is assumed to be isotropic and parabolic, with a single LH effective mass of $0.044m_0$, which is sufficiently accurate for modeling the occupancy of the band under high electric fields.

We have also simulated the electron and hole mobility as a function of n-type and p-type doping concentrations, respectively, achieving very good agreement with the experimental data trends. The electron (hole) relaxation time decreases significantly from 0.44 ps (0.18 ps) to 0.001 ps (0.06 ps) at the highest electric fields of 700 kV cm^{-1} (for electrons) and 10 kV cm^{-1} (for holes), reflecting the substantial increase in electron and hole velocity, which is desirable for nanoscale multigate transistors. This large electron and hole velocity is a result of the highly anisotropic electron L-valley and the HH band, with a nearly 19-fold and 32-fold difference, respectively, between the longitudinal and transverse effective masses. At higher electric fields of 20 kV cm^{-1} (for electrons) and 2 kV cm^{-1} (for holes), the increase in the occupancy of the subsequent valley or band—namely, the Γ-valley for electrons and the LH band for holes—affects the electron and hole drift velocities. Additionally, at high electric fields, the hole transitions from the HH band to the LH band, increasing the occupancy of the LH band with its smaller effective mass, which further enhances the average hole velocity. The high carrier velocity in Ge makes it an extremely promising channel material for future n-type and p-type CMOS transistor generations, as previously recognized.[70,71] While the present MC simulations treat electrons and holes separately in unipolar devices, the approach can be adapted into a multiparticle framework to enable simultaneous carrier transport in bipolar devices.

ORCID

Aynul Islam https://orcid.org/0000-0002-3825-1484
Shuqiao Cai https://orcid.org/0009-0009-5520-8734
Murad Alabdullah https://orcid.org/0000-0002-4941-2474
Karol Kalna https://orcid.org/0000-0002-6333-9189

References

1. J. E. Smith, *Phys. Rev.*, **178**, 1364 (1969).
2. J. P. Nougier and M. Rolland, *Phys. Rev. B*, **8**, 5728 (1973).
3. L. Reggiani, C. Canali, F. Nava, and G. Ottaviani, *Phys. Rev. B*, **16**, 2781 (1977).
4. C. Jacoboni and L. Reggiani, *Rev. Mod. Phys.*, **55**, 645 (1983).
5. M. V. Fischetti, *IEEE Trans. Electron Devices*, **38**, 634 (1991).
6. J. Lindberg, M. Aldegunde, D. Nagy, W. G. Dettmer, K. Kalna, A. J. Garcìa-Loureiro, and D. Perić, *IEEE Trans. Electron Devices*, **61**, 423 (2014).
7. D. Nagy, G. Indalecio, A. J. García-Loureiro, M. A. Elmessary, K. Kalna, and N. Seoane, *IEEE J. Electron Devices Soc.*, **6**, 332 (2018).
8. D. Nagy, G. Espiñeira, G. Indalecio, A. J. García-Loureiro, K. Kalna, and N. Seoane, *IEEE Access*, **8**, 53196 (2020).
9. C. Riddet, J. R. Watling, K.-H. Chan, E. H. C. Parker, T. E. Whall, D. R. Leadley, and A. Asenov, *IEEE Trans. Electron Devices*, **59**, 1878 (2012).
10. D. Lin, G. Brammertz, S. Sioncke, C. Fleischmann, A. Delabie, K. Martens, H. Bender, T. Conard, W. Tseng, and J. Lin, *IEDM Tech. Dig.*, *2009 IEEE International Electron Devices Meeting*327 (2009).
11. M. Heyns, A. Alian, G. Brammertz, M. Caymax, Y. Chang, L. Chu, B. De Jaeger, G. Eneman, F. Gencarelli, and G. Groeseneken, *IEDM Tech. Dig.*, *2011 International Electron Devices Meeting*299 (2011).
12. P. H. Beton and A. F. J. Levi, *Appl. Phys. Lett.*, **55**, 250 (1989).
13. R. Hathwar, Y. Zou, C. Jirauschek, and S. M. Goodnick, *J. Phys. D: Appl. Phys.*, **52**, 093001 (2019).
14. M. B. Prince, *Phys. Rev.*, **92**, 681 (1953).
15. T. Krishnamohan, D. Kim, T. V. Dinh, A.-T. Pham, B. Meinerzhagen, C. Jungemann, and K. C. Saraswat, *IEDM Tech. Dig.*, 899 (2008).
16. D. Kuzum, A. J. Pethe, T. Krishnamohan, and K. C. Saraswat, *IEEE Trans. Electron Devices*, **56**, 648 (2009).
17. S. Takagi and M. Takenaka, *VLSI Symp. Tech. Dig.*147 (2010).
18. M. Myronov, K. Sawano, and Y. Shiraki, *Appl. Phys. Lett.*, **94**, 042106 (2009).
19. J. Mitard et al., *Jpn. J. Appl. Phys.*, **50**, 04DC17 (2011).
20. R. Lee et al., *IEEE Electron Device Lett*, **42**, 962 (2021).
21. W. M. Weber, L. Wind, A. Fuchsberger, R. Behrle, D. Nazari, J. Aberl, E. P. Navarrete, M. Brehm, and M. Sistani, *Proc. IEEE Nanotechnol. Mater. Devices Conf.* 446 (2023).
22. W.-H. Hsieh, Y.-R. Chen, Y.-C. Liu, Z. Zhao, J.-Y. Lee, C.-T. Tu, B.-W. Huang, J.-F. Wang, M. H. Lee, and C. W. Liu, *IEEE Trans. Electron Devices*, **71**, 1758 (2024).
23. Y.-W. Lin, S.-W. Lin, B.-A. Chen, and C.-J. Sun, *IEEE J. Electron Devices Soc.*, **11**, 480 (2023).
24. Y.-W. Lin, B.-A. Chen, K.-W. Huang, B.-X. Chen, G.-L. Luo, Y.-C. Wu, and F.-J. Hou, *IEEE Electron Device Lett*, **45**, 2013 (2024).
25. G. Ottaviani, L. Reggiani, C. Canali, F. Nava, and A. Alberigi-Quaranta, *Phys. Rev. B*, **12**, 3318 (1975).
26. L. Reggiani, *J. Phys. Chem. Solids*, **37**, 293 (1976).
27. T.-S. Liou, T. Wang, and C.-Y. Chang, *J. Appl. Phys.*, **76**, 4749 (1994).
28. M. V. Fischetti and S. E. Laux, *J. Appl. Phys.*, **80**, 2234 (1993).
29. F. M. Bufler, P. Graf, B. Meinerzhagen, G. Fischer, and H. Kibbel, *J. Vac. Sci. Technol. B*, **16**, 1667 (1998).
30. N. Seoane, D. Nagy, G. Indalecio, G. Espiñeira, K. Kalna, and A. J. García-Loureiro, *Materials*, **12**, 2391 (2019).
31. L. I. Schiff, *Quantum Mechanics* (McGraw-Hill, New York) (1968).
32. S. E. Laux and F. Stern, *Appl. Phys. Lett.*, **49**, 91 (1986).
33. A. Islam, B. Benbakhti, and K. Kalna, *IEEE Trans. Nanotechnol.*, **10**, 1424 (2011).
34. F. R. Pierret, *Advanced Semiconductor Fundamentals* (Pearson Education Inc., New Jersey) 2nd ed. (2003).
35. E. O. Kane, *J. Phys. Chem. Solids*, **1**, 82 (1956).
36. K. Seeger, *Semiconductor Physics* (Springer, Berlin) (1991).
37. D. A. Neamen, *Semiconductor Physics and Devices: Basic Principles* (McGraw-Hill Education, New York) 4th ed. (2012).
38. C. Jacoboni and L. Reggiani, *J. Phys. Colloques*, **42**, C7 (1981).
39. C. Jacoboni, C. Canali, G. Ottaviani, and A. Alberigi Quaranta, *Solid-State Electron*, **20**, 77 (1977).
40. S. M. Sze and K. K. Ng, *Physics of Semiconductor Devices* (Wiley, Hoboken, NJ) 3rd ed. 26 (2006).
41. M. Cardona and F. H. Pollak, *Phys. Rev.*, **142**, 530 (1966).
42. C. Kittel, *Introduction to Solid State Physics* (Wiley, Hoboken, NJ) 8th ed.28 (2005).
43. M. Cardona and P. Y. Yu, *Fundamentals of Semiconductors* (Springer, Berlin) 4th ed. (2010).
44. B. J. Van Zeghbroeck, *Principles of Semiconductor Devices and Heterojunctions* (Prentice Hall, Upper Saddle River, N.J., London) 1st ed. (2010).
45. M. Lundstrom, *Fundamentals of Carrier Transport* (Cambridge University Press, Cambridge) 2nd ed. (2000).
46. B. K. Ridley, *Quantum Processes in Semiconductors* (Oxford University Press, Oxford) 1st ed. (1982).
47. B. Nag, *Electron Transport in Compound Semiconductors* (Springer-Verlag, New York) 1st ed. (1980).
48. C. Kittel, *Quantum Theory of Solids* (Wiley, New York) 1st ed. (1963).
49. K. Tomizawa, *Numerical Simulation of Submicron Semiconductor Devices* (Artech House, London) (1993).
50. J. D. Wiley, *Phys. Rev. B*, **4**, 2485 (1971).
51. G. L. Bir and G. E. Pikus, *Sov. Phys. Solid State*, **2**, 2039 (1961).
52. M. Costato and L. Reggiani, *Phys. Status Solidi B*, **58**, 71 (1973).
53. R. W. Kelsall, *Monte Carlo Simulations of Hole Transport and Relaxation in the Valence Bands of a Semiconductor Quantum Well*, University of Leeds, UK (1989), Ph.D. Thesis.
54. L. Reggiani, C. Canali, F. Nava, G. Ottaviani, and P. Lawaetz, *Proc. Int. Conf. Phys. Semicond.*12, 819 (1974).
55. O. Madelung, *Introduction to Solid-State Theory* (Springer, Heidelberg) 2nd ed. (1981).

56. D. K. Ferry, *Semiconductors: Bonds and Bands* (IOP Publ., Bristol) 2nd ed. (2019).
57. E. M. Conwell and V. Weisskopf, *Phys. Rev.*, **77**, 388 (1950).
58. H. Brooks, *Phys. Rev.*, **83**, 879 (1951).
59. B. K. Ridley, *J. Appl. Phys.*, **48**, 754 (1977).
60. L. Hrivnák, V. Bezák, J. Foltìn, and M. Ozvold, *Theory of Solid State* (Veda, Bratislava) 2nd ed. (1985).
61. H. Brooks, *Advances in Electronics and Electron Physics*, ed. L. Marton (Academic Press, New York) 7, 85 (1955).
62. P. Debye and E. Hückel, *Phys. Z.*, **24**, 185 (1923).
63. A. Islam and K. Kalna, *Semicond. Sci. Technol.*, **26**, 055007 (2011).
64. D. M. Szmyd, P. Porro, and A. Majerfeld, *J. Appl. Phys.*, **68**, 2367 (1990).
65. M. V. Fischetti, *J. Appl. Phys.*, **89**, 1232 (2001).
66. A. A. Abrikosov, P. L. Gorkov, and I. E. Dzyaloshinski, *Methods of Quantum Field Theory in Statistical Physics* (Dover Publications, New York) (1975).
67. P. Borowik and J.-L. Thobel, *J. Appl. Phys.*, **84**, 3706 (1998).
68. P. H. Nguyen, K. R. Hofmann, and G. Paasch, *J. Appl. Phys.*, **94**, 375 (2003).
69. M. Sánchez, *Z. Naturforsch. A*, **23**, 2035 (1968).
70. Y. Kamata, *Mater. Today*, **11**, 30 (2008).
71. R. Zhang, P.-C. Huang, J.-C. Lin, N. Taoka, M. Takenaka, and S. Takagi, *IEEE Trans. Electron Devices*, **60**, 927 (2013).